Nanoscale

Accepted Manuscript

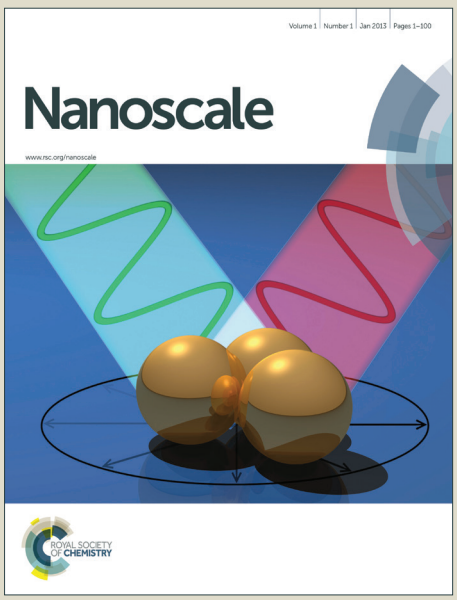

ROYAL SOCIETY OF CHEMISTRY

www.rsc.org/nanoscale

Nanoscale

ARTICLE

Coaxial $CoMoO_4$ Nanowire Arrays with Chemically Integrated Conductive Coating for High-Performance Flexible All-Solid-State Asymmetric Supercapacitors

Received 00th January 20xx,
Accepted 00th January 20xx

DOI: 10.1039/x0xx00000x

www.rsc.org/

Yaping Chen,[a] Borui Liu,[b] Qi Liu,[a,*] Jun Wang,[a,c,*] Zhanshuang Li,[a] Xiaoyan Jing,[a] and Lianhe Liu,[a,c]

Flexible all-solid-state supercapacitors have offered promising applications as novel energy storage devices based on their merits, such as small size, low cost, light weight and highly wearability for high-performance portable electronics. However, one major challenge to make flexible all-solid-state supercapacitors depends on the improvement of electrode materials with higher electrical conductive property and longer cycling stability. In this article, we put forward a simple strategy to *in-situ* synthesize 1D $CoMoO_4$ nanowires (NWs), using highly conductive CC and electrical conductive PPy wrapping layer on $CoMoO_4$ NW arrays for high performance electrode materials. The results show that $CoMoO_4$/PPy hybrid NWs electrode exhibits a high areal specific capacitance of ca. 1.34 F cm^{-2} at a current density of 2 mA cm^{-2}, which is remarkably better than the corresponding values for pure $CoMoO_4$ NWs electrode of 0.7 F cm^{-2}. An excellent cyclic performance of nanocomposites of up to 95.2% (ca. 1.12 F cm^{-2}) is achieved after 2000 cycles compared to pristine $CoMoO_4$ NWs. In addition, we fabricate flexible all-solid-state ASC which can be cycled reversibly in the voltage range of 0–1.7 V, and exhibits maximum energy density of 104.7 Wh kg^{-1} (3.522 mWh cm^{-3}), demonstrating a great potential for practical applications in flexible energy storage electronics.

Introduction

The ever-increasing societal demand for large-scale energy storage applications in portable electronics and hybrid electric vehicles has spurred on significant research efforts for the next-generation of high-performance electrochemical rechargeable devices. High energy storage lithium-ion batteries and supercapacitors are considered as ideal candidates. Unlike batteries, which deliver energy slowly because of their rate-limiting faradaic reactions, supercapacitors store electric power in electrochemically active materials or at the interfacial region of the electrode/electrolyte and, therefore, provide much faster charge/discharge rates as well as much longer cycling life, demonstrating their advantageous characteristics in high-power energy consumption applications.[1-5]

It is well known that electrode materials play a vital role in supercapacitor performance. Conventional carbon-based materials, including mesoporous carbon and graphene (or reduced graphene oxides) with modification of surface chemical functional groups have exhibited excellent supercapacitor properties, specifically for electric double-layer capacitors (EDLCs).[6] Compared with carbon-based materials, transition metal oxides (TMOs) materials (unitary and binary) are based on pseudocapacitive characteristics; these include Co_3O_4,[7] MnO_2,[8] RuO_2,[9] NiO[10] and V_2O_5,[11] and binary TMOs such as $NiCo_2O_4$,[12] $MnMoO_4$,[13] $CoMoO_4$,[14] $ZnCo_2O_4$,[15] and $NiMoO_4$[16] and so forth. In particular, $CoMoO_4$ as one of the family of metal-molybdates, possesses distinctive reversible and electrochemical capacitive properties, in terms of chemical stability, low cost, high specific capacitance and energy density, but rarely studied in the flexible supercapacitor context. Electrically conducting polymers, such as polyaniline (PAni),[17] polypyrrole (PPy),[18, 19] poly(ethylenedioxythiophene) (PEDOT) and their derivatives,[20] are mixed with or electrochemically deposited onto transition metal oxides to achieve high-performance hybrid electrode materials. Because of the promising potential for electrochemical active materials, a key strategy is to adopt the use of the aforementioned materials as active electrodes directly to improve cyclic performance and rate performance by a rational design of synthesis and control of the microscopic architectures.[21, 22]

Supercapacitors are a unique class of energy-storage devices that can operate at a much higher power density than conventional batteries. One emerging application is in electric/hybrid heavy and consumer automotive vehicles, which can employ a high power device to supply a surge during

[a] Key Laboratory of Superlight Material and Surface Technology, Harbin Engineering University, Harbin, 150001, P.R. China. E-mail: zhqw1888@sohu.com
[b] Department of Mechanical Engineering, The University of Texas at Austin, Austin, TX, 78712, United States.
[c] Institute of Advanced Marine Materials, Harbin Engineering University, 150001, PR China.

† Electronic Supplementary Information (ESI) available: See DOI: 10.1039/x0xx00000x

startup (heavy) and to convert the kinetic energy associated with vehicle braking into useful electricity (consumer automotive).[23] However, the current pseudocapacitor technology is limited by a considerably lower energy density, which is more than one order of magnitude smaller than that Li-ion batteries while larger than that ideal supercapacitor.[24, 25] Nanoscience and technology, as focal areas of research, are bringing revolutionary opportunities to meet the needs for more efficient electrical energy storage and conversion materials for all kinds of application. In contrast to bulk materials, nanomaterials, have exhibited distinct chemical and physical characteristics in electrochemical energy storage devices, for instance offering a large surface area to enhance the electrochemical reaction or molecular adsorption occurring at the solid-liquid or solid-gas interface as well as rendering high crystallinity and/or porous structure pathways to facilitate electron or ion transport, and so guaranteeing a high efficiency of the electrochemical process.[26-28] Among the various nanostructures, one-dimensional (1D) nanostructures, such as nanowires, have drawn wide-ranging interest due to their special functional features. 1D nanowire structures offer many merits as listed briefly follows: (1) Nanowires provide a direct current channel, taking greater advantage of electrical transport than particle electrodes. (2) 1D nanowires can effectively enhance the specific surface area of the electrode and significantly shorten the charge migration distance, thus diminishing the ionic/electronic transport impedance and reducing the charge-discharge time to improve the power supplying capability at high rates.[29, 30] (3) The design of 1D nanowires structure avoids volume expansion and limits mechanical degradation, offering long-life cycling.[31, 32] (4) Nanowires could directly germinate on metallic or carbonic substrate surface with the additive-free and binder-free as uniform arrays. (5) Nanowires can realize framework support to construct intricate and multifunctional architectures, achieving the advantages of each subunit.[33-35] In the past few years, promising efforts have been made to explore various types of structures, such as H-TiO_2@MnO_2//H-TiO_2@C core–shell nanowires,[36] ZnO@CuS@PEDOT core@shell nanorod arrays decorated with MnO_2 nanoparticles,[37] MOF-Derived ZnO@ZnO quantum dots/C core-shell nanorod arrays on a carbon cloth,[38] these have been successfully reported to significantly enhance electrochemical performance when used as electrode materials for supercapacitors.

Herein, we design and synthesize 1D core-shell nanowire arrays onto flexible conductive substrates using a facile two-step solution-based method for high performance asymmetric supercapacitors (ASC). PPy is wrapped firmly onto the outer surface of $CoMoO_4$ nanowires to form $CoMoO_4$/PPy core-shell hierarchical nanostructures, which not only provide good strain accommodation, but also achieve a free-binder assembly of flexible SC devices. The electrochemical performance was experimentally investigated and found favorable. The hybrid NWs give rise to high area capacitance up to ca. 1.34 F cm^{-2} at a charge/discharge current density of 2 mA cm^{-2}. Robust long-term cycling performance shows ca. 95.2% capacitance retention after 2000 cycles with an average coulombic efficiency of over 99.5%. In addition, the flexible all-solid-state asymmetric supercapacitor (ASC) device exhibits a high energy density and power density up to 104.7 Wh kg^{-1} (3.522 mWh cm^{-3}) and 971.43 W kg^{-1} (32.6 mW cm^{-3}) at a current density of 4 mA cm^{-2}, respectively. The desirable results suggest such a supercapacitor electrode of $CoMoO_4$/PPy core shell hybrid NW arrays has with great prospects for high-performance energy-storage utilities.

Experimental

Synthesis of $CoMoO_4$ NW arrays on CC

Prior to the synthesis, commercial CC pieces (Phychemi Company Limited, 40 mm × 40 mm × 1 mm in size) were first ultrasonic-treated in acetone and ethanol mixture, then cleaned by deionized (DI) water and dipped in 6 M nitric acid solution overnight and rinsed successively by DI water, followed by drying under Ar flow at 60 °C for 5 h. In a typical synthetic process, the precursor solution was blended with 5 mmol of $Co(NO_3)_2 \cdot 6H_2O$ and 5 mmol of $Na_2MoO_4 \cdot 7H_2O$ in 50 mL of DI water under constant magnetic stirring to form a uniform light purple solution. The washed CC substrates and precursor reaction solution were together transferred into an 80 mL Teflon-lined stainless steel autoclave and reacted at 180 °C for 10 hours. The autoclave was cooled down to room temperature naturally, and the resulting samples collected and rinsed with DI water mixture several times before drying in a vacuum oven at 60 °C overnight. Finally, to obtain $CoMoO_4$ NWs, the dried samples were annealed at 300 °C for 1 h in Ar protection at a ramping rate of 5 °C per minute.

Preparation of $CoMoO_4$/PPy core–shell NW arrays

Pyrrole (Sigma-Aldrich, 99%) was first distilled under vacuum to remove the oxidation impurities. PPy was wrapped onto the $CoMoO_4$ nanowires by an oxidative cationic polymerization process. The purified p-TSA 0.416 g was dissolved in 30 mL ethanol solution followed by continuous vigorous stirring in an ice-water bath (0–4 °C) for 5 min before adding pyrrole monomer (0.2 mL) with magnetic stirring for 1 min (solution A). Subsequently, 0.24 g ammonium persulfate (APS) was dissolved in 20 ml DI water under constant magnetic stirring to form a transparent solution which was then rapidly transferred into solution A and stirred for 30 s (solution B). Next, the prepared $CoMoO_4$/CC composites were added into solution B. The polymerization was performed in the dark for 4 h. Then the sample was collected and rinsed several times with ethanol/DI water mixture (50:50, v/v). Finally, the as-prepared $CoMoO_4$/PPy NW arrays on CC electrode ($CoMoO_4$/PPy/CC) were dried under vacuum at 60 °C for 5 h.

Materials characterizations

The crystalline structures of the as-prepared electrode materials were determined using a powder X-ray diffraction system (XRD; RigakuTTR-III) equipped with Cu Kα radiation (λ = 0.15406 nm). The absorption spectrum was measured by a Fourier transform infrared spectrometer (FT-IR spectra;

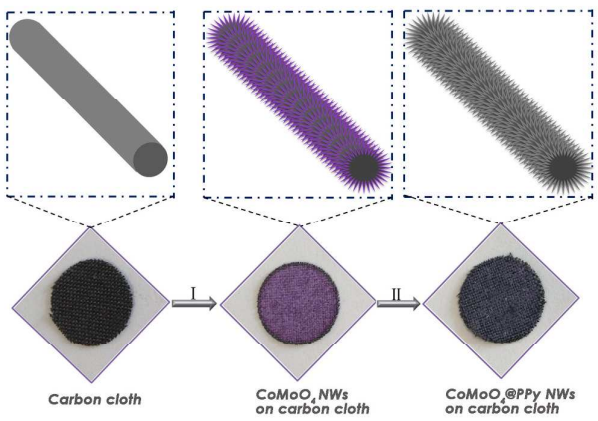

Fig. 1 Schematic illustration of the growth process of the hybrid nanostructured $CoMoO_4$/PPy/CC electrode. Corresponding digital images of pristine CC, $CoMoO_4$/CC, and $CoMoO_4$/PPy/CC nanocomposite electrodes, respectively.

PerkinElmer Spectrum 100). The topographic characteristics of the electrodes were examined by scanning electron microscopy (SEM; JEOL JSM-6480A microscope) and transmission electron microscopy (TEM; Philips CM 200 FEG, 160 kV).

Electrochemical measurements

Fresh $CoMoO_4$/PPy/CC hybrid electrodes (10 mm × 15 mm, effective projected area of 10 mm × 10 mm) were directly used as working electrodes. A platinum foil (1 cm × 1 cm) acted as the counter electrode and a saturated calomel electrode (SCE) as the reference electrode. All experiments were carried out at room temperature. 2.0 M KOH aqueous solution served as the electrolyte after purging with high-purity nitrogen gas for 30 min. The electrochemical measurements were carried out on a CHI 660D electrochemistry workstation. Cyclic voltammetry (CV) tests were conducted in a potential range of 0−0.5 V (versus SCE) at sweep rates of 5–100 mV s^{-1}. The constant current charge/discharge tests were carried out at various current densities within a potential range of 0−0.5 V (versus SCE), and the cycling behavior was characterized up to 2000 cycles. Electrochemical impedance spectroscopy (EIS) was performed to determine the capacitive performance at open circuit voltage (OCV) with a frequency range of 0.01−10^5 Hz. These electrochemical measurements were performed on a three-electrode system.

Assembly of the all-solid-state ASC

Generally, an all-solid-state ASC was fabricated by a $CoMoO_4$/PPy hybrid NWs electrode as the positive electrode and an activated carbon/CC (AC, Sigma-Aldrich) electrode as the negative electrode. The $CoMoO_4$/PPy hybrid electrode was resized to a rectangular shape (1.0 cm × 2.0 cm in size) with average mass loading of 1.5−1.8 mg cm^{-2}. The negative electrode was prepared by homogeneously mixing 80 wt.% commercial AC, 10 wt.% carbon black powder, and 10 wt.% polytetrafluoroethylene (PTFE) and blade casting the mixture onto a piece of carbon cloth (1.0 cm × 2.0 cm in size) with mass loading tuned to gain the best performance. Then, the PVA-KOH gel electrolyte was prepared by mixing as-prepared 6 g polyvinyl alcohol (PVA) with 3 g KOH in 60 ml of deionized water and heated at 80 °C under stirring for 2 h until it became homogeneously clear. A parafilm-sealed glass vial was used to prepare the ultrathin KOH/PVA films after a drying process at 40 °C for 2 h. Afterward, the ASC device was assembled by sandwiching PVA-KOH gel electrolyte film between the AC/CC and $CoMoO_4$/PPy/CC electrodes under mechanical stress. The specific capacitance (C_{sp}), energy density, and power density of the ASC were all calculated based on the total mass of both negative and positive electrodes excluding the weights of current collectors. The thickness of the as-assembled all-solid-state ASC was measured to be ca. 1.03~1.05 mm. All electrochemical tests of ASC device were performed in a two-electrode configuration at ambient temperature.

Data Analysis

Data analysis included specific capacitance, energy density, and power density of supercapacitor devices. The specific capacitance C_{sp} (F cm^{-2}) of the electrochemical supercapacitor device was calculated in the three (two)-electrode configuration using the following formulas:

$$C_{sp} = \frac{C}{A} = \frac{I_d t}{V}$$

where C_{sp} is the specific capacitance of the supercapacitor, A is the effective projected area of the electrodes, I_d is the current

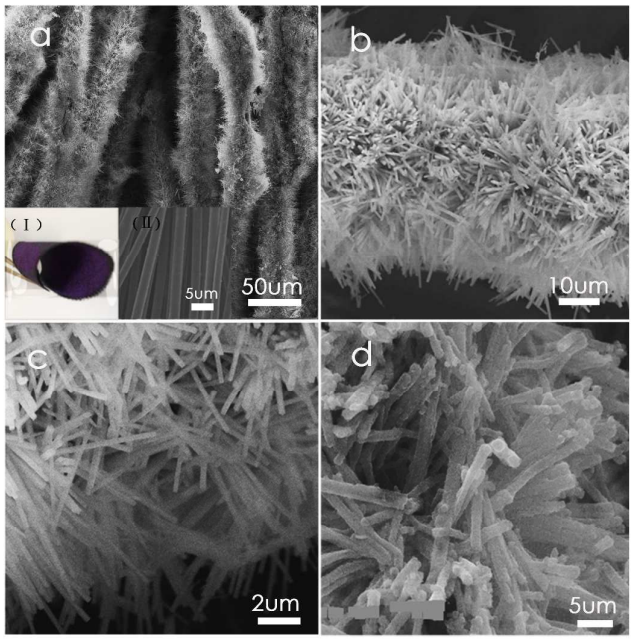

Fig. 2 (a) Typical FESEM images of the $CoMoO_4$ NW arrays growing on carbon cloth at low magnification. Inset in panel (a): (Ⅰ) Photographic image of $CoMoO_4$/CC electrode exhibiting very good flexibility (can be rolled up with tweezers). (Ⅱ) bare carbon fibers. (b-c) High-magnification images of pristine $CoMoO_4$ NW arrays on CC. (d) Zoom–in image of $CoMoO_4$/PPy core-shell NW arrays on CC.

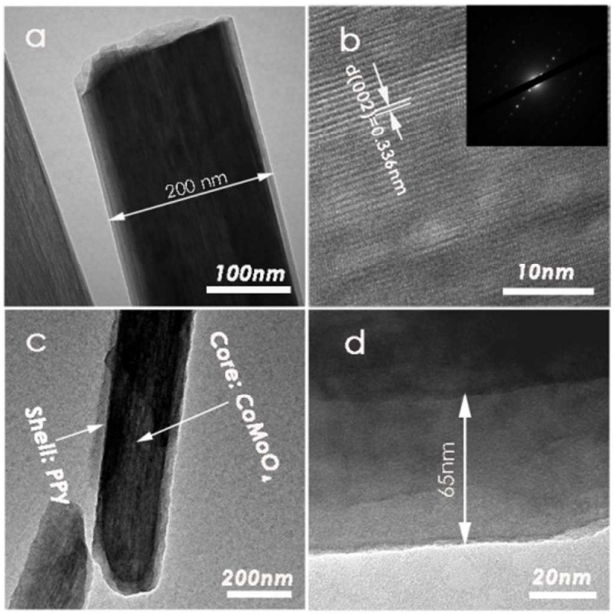

Fig. 3 (a,c) TEM images of single $CoMoO_4$ and $CoMoO_4$/PPy core-shell NW. (b) High resolution TEM image of pure $CoMoO_4$ NW. The inset in panel (b): SAED pattern of pristine $CoMoO_4$ NW. (d) High magnification TEM images of $CoMoO_4$/PPy core-shell NW.

density based on effective projected area of the electrodes, t is constant-current discharging time, and V is the applied potential range. Energy density and power density are calculated by using the following equations

$$\boldsymbol{P = \frac{V^2}{4Rm}} \quad \& \quad \boldsymbol{E = \frac{C_{sp}V^2}{2m}}$$

where V is the applied potential range, R is the internal resistance, m is the effective active mass loading of the electrodes, and C_{sp} is the measured specific capacitance of the supercapacitors.

Results and discussion

A schematic illustration of the synthesis of the flexible hybrid $CoMoO_4$/PPy core-shell NW arrays on CC supercapacitor electrode is presented in Figure 1. In the first step, $CoMoO_4$ NW arrays are grown directly onto a carbon fiber substrate via a facile and scalable hydrothermal route (step I). Subsequently, conductive PPy layers are coaxially deposited onto $CoMoO_4$ NWs surface (step II). The digital photos clearly show the color changing of the electrode at the three stages of preparation. The black sample is pre-treatment pristine carbon fiber, the purple and gray ones are $CoMoO_4$/CC and $CoMoO_4$/PPy/CC, respectively.

The morphological characteristics of $CoMoO_4$ NW arrays on CC electrode were demonstrated by a SEM technique, as shown in Figure 2. Figure 2a clearly displays the well-established and uniform $CoMoO_4$ NW arrays grown on the large area of carbon fibers. allowing high loading capability of the active materials. The product still keeps the ordered fibrous structure of the carbon fiber templates as shown in the original carbon fibers of the inset (II) in Figure 2a. The inset (I) shows a photographic image of the $CoMoO_4$/CC hybrid electrode, exhibiting excellent flexibility and outstanding mechanical stability. It can be readily rolled up and back and forth with tweezers, making it possible for further flexible device applications. Higher-magnification SEM images shown in Figure 2b-c provide distinct information about the $CoMoO_4$ products. From Figure 2b, we see an individual carbon microfiber anchored with numerous $CoMoO_4$ NW arrays, allowing high loading capability of the active materials. Typical $CoMoO_4$ nanowires have uniform diameters of about 180−200 nm and relatively random lengths as seen from Figure 2c. In comparison to Figure 2c, Figure 2d apparently reveals the PPy conductive coating on the original $CoMoO_4$ NWs, confirming the maintenance of the previous core-shell nanoarray morphology. Also, we observe that the conductive PPy does not obstruct the interspace of the electrode and no break occurs during the polymerization process, guaranteeing good electrode/electrolyte contact and no hindrance to the charge transportation routes.

The detailed structure and morphology of these nanoarrays were further obtained from TEM (Figure 3). Figure 3a reveals the low-magnification TEM image of a typical individual $CoMoO_4$ NW with a diameter of ca. 200 nm. The high-resolution TEM (HRTEM) image shown in Figure 3b reveals the lattice spacing of ca. 0.336 nm corresponding well to the (002) planes of $CoMoO_4$. Also, the selected area electron diffraction (SAED) pattern of the pure $CoMoO_4$ structures shows a well-defined lattice (in the inset of Figure 3b) confirming the polycrystalline characteristic of $CoMoO_4$. Figure 3c shows clearly the core-shell structure $CoMoO_4$/PPy NW, indicating that the PPy conductive layer has been uniformly wrapped onto $CoMoO_4$ NWs. The thickness of the outer shell is about 65 nm. As a result, the PPy shell will likely avoid the aggregation and volume changing of $CoMoO_4$ NWs.

The results of XRD and FT-IR spectrum of pristine $CoMoO_4$, PPy, and $CoMoO_4$/PPy core-shell NWs are exhibited in Figure 4. The crystal structure of the $CoMoO_4$ NWs, PPy and $CoMoO_4$/PPy hybrid nanocomposite have been evidently revealed by XRD analytical patterns in Figure 4a. The obtained XRD pattern from the blue diffractive peaks confirms the

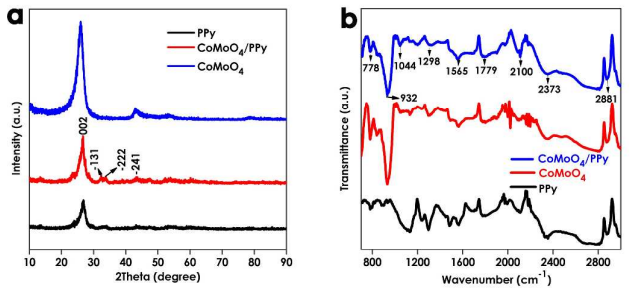

Fig. 4 (a) XRD and (b) FT-IR results of pure $CoMoO_4$, PPy, and $CoMoO_4$/PPy core-shell NWs nanocomposite electrode.

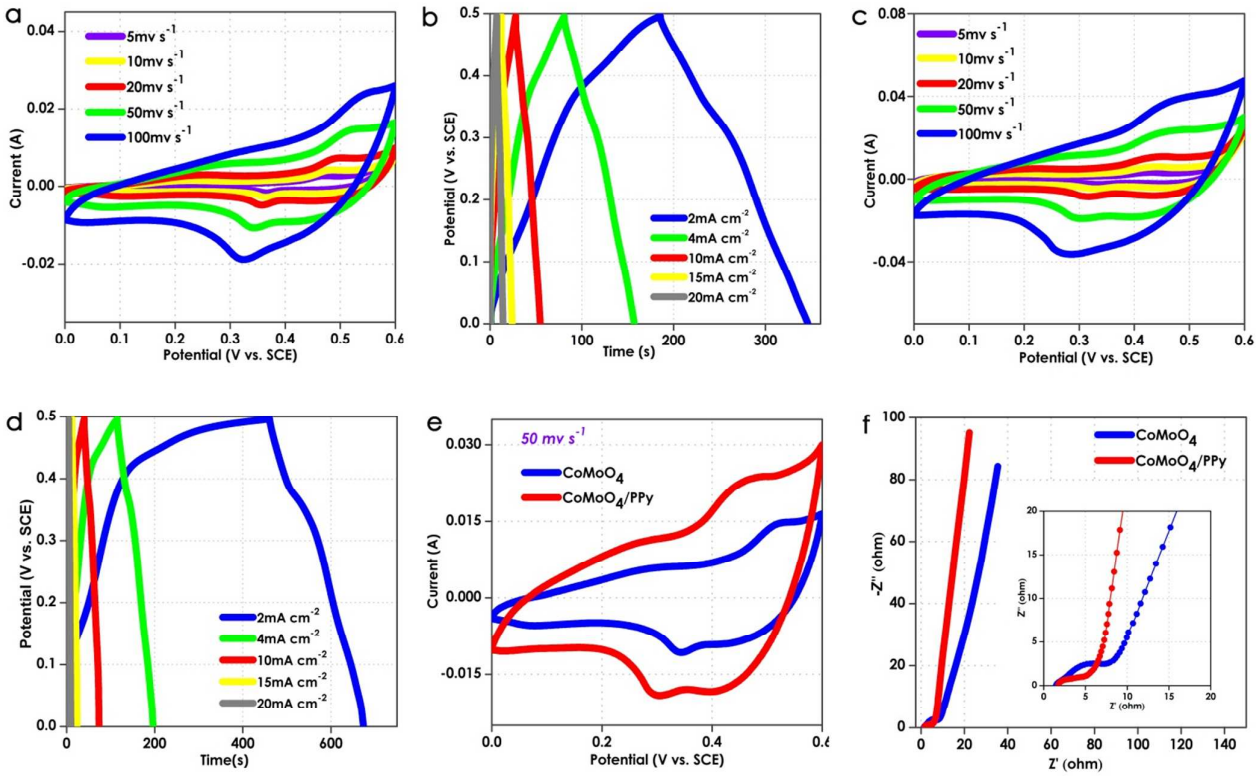

Fig. 5 Electrochemical performance of pure $CoMoO_4$ and $CoMoO_4$/PPy core-shell NWs nanocomposite electrode. (a) Cyclic voltammetry at different scan rates (5–100 mV s^{-1}) in 2.0 M KOH aqueous electrolyte and (b) galvanostatic charge–discharge profiles at various current densities of 2, 4, 10, 15, and 20 mA cm^{-2} of pristine $CoMoO_4$/CC electrode. (c) CV curves at different scan rates (5–100 mV s^{-1}) in 2.0 M KOH aqueous electrolyte and (d) Galvanostatic charge/discharge measurement at various current densities of 2, 4, 10, 15, and 20 mA cm^{-2} for $CoMoO_4$/PPy/CC hybrid NWs array electrode. (e) CV graphs of the $CoMoO_4$ NWs/CC and $CoMoO_4$/PPy/CC hybrid NW arrays electrodes at scan rate of 50 mV s^{-1} operated within the potential window of 0–0.6 V. (f) Initial EIS plots of the $CoMoO_4$ NWs/CC and $CoMoO_4$/PPy/CC hybrid NW arrays electrodes at open circuit voltage (OCV). Z'': imaginary impedance, Z': real impedance.

characteristic diffraction peaks of $CoMoO_4$ (JCPDS card no. 21-0868), demonstrating the lattice parameters observed are well matching the PDF card. The characteristic peaks are observed in the black pattern in accordance with the XRD pattern of PPy reported by the earlier reports.[39] In the red part, one significant diffraction peak at around 26° was observed, resulting from the $CoMoO_4$ core and PPy shell.aa The core-shell structure $CoMoO_4$/PPy hybrid nanocomposite is observed to display all the characteristic peaks corresponding to $CoMoO_4$ and PPy separately, confirming free of impurities phases in the nanocomposites. The chemical composition of the hybrid materials was also confirmed by FT-IR spectra. The most obvious absorption peaks at 778, 932 and 1044 cm^{-1} are attributed to the aromatic out-of-plane C−H and Mo−O deformation vibration. Furthermore, the band at 1298 cm^{-1} is induced by C–N stretching vibrations. Absorption peaks at 1779 and 1565 cm^{-1} C=C and C−N on the pyrrole ring, respectively. Two evident absorptions at 2373 and 2881 cm^{-1} can be ascribed to the $-C{\equiv}N^{+}-O$ and $-N^{+}{\equiv}C^{-}-$ stretching vibrations. A broad band at about 2800 cm^{-1} may be due to −CHO in-plane vibrations or O−H formation. Therefore, the shell obtained after oxidative cationic polymerization is PPy.

To study the pseudocapacitive activities of the highly ordered $CoMoO_4$ NW arrays and $CoMoO_4$/PPy hybrid NW arrays as supercapacitor electrodes, we directly apply a three-electrode configuration, which is composed of the pristine $CoMoO_4$/CC electrode and $CoMoO_4$/PPy/CC electrode as the active electrodes separately for CV and galvanostatic charge/discharge measurements in 2.0 M KOH aqueous

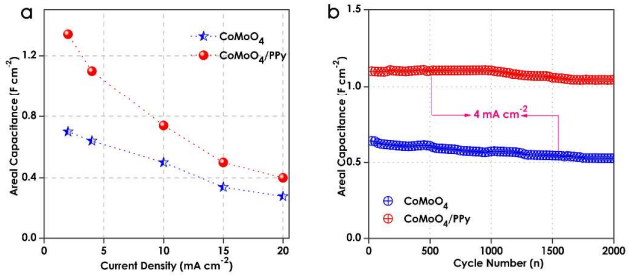

Fig. 6 (a) Areal capacitance as a function of current density for $CoMoO_4$/CC and $CoMoO_4$/PPy/CC electrode. The area of each sample was 1 cm^{-2}. (b) Cycling performance of $CoMoO_4$/CC and $CoMoO_4$/PPy/CC electrode at a current of 4 mA cm^{-2} for 2000 cycles in 2 M KOH aqueous electrolyte.

electrolyte (Figure 5). Figure 5a shows the cyclic voltammetry (CV) of pristine $CoMoO_4$ NWs/CC electrode under different scan rates from 5 to 100 mV s^{-1} in a potential range of 0−0.6 V versus an SCE. The CV curves demonstrate a typical pseudocapacitive-type behavior, resulting from pristine $CoMoO_4$ NW arrays. The pair of redox peaks shown in CV curves is ascribed to the reversible redox reaction of Co (II) ↔ 2Co (III) + e^-. The anodic peaks shift to higher potential while the cathodic peaks shift to lower potential as the increased scan rate due to triggered by the auxetic overpotential. The galvanostatic charge-discharge (GCD) curves of the $CoMoO_4$/CC electrode at different current rates of 2−20 mA cm^{-2} within the potential range of 0−0.5 V. (Figure 5b) imply a high efficiency of the pseudocapacitor and the occurrence of a fast reversible redox reaction.. The inconspicuous charge and discharge voltage plateaus at around 0.4 V and 0.3 V are in consistent with the electrochemical behavior of the CV curves, respectively, again confirming the pseudocapacitive properties of the electrode. Figure 5c shows the CV curves of the $CoMoO_4$/PPy/CC electrode, which are agree well with those of the $CoMoO_4$/CC electrode. However, it is noticeable that the peak-current values of the $CoMoO_4$/CC electrode are narrower than those of the $CoMoO_4$/PPy/CC hybrid electrode. This may be largely ascribed to the conductive PPy coating offering enhanced electrical conductivity to accommodate the poor electrical conductivity of the double-metal oxides NWs. Figure 5d illustrates GCD profiles of $CoMoO_4$/PPy/CC hybrid electrode measured at the current densities from 2 to 20 mA cm^{-2}. Compared to $CoMoO_4$/CC electrode, the areal capacitance of the $CoMoO_4$/PPy/CC hybrid electrode is improved (0.7 and 1.34 F cm^{-2} at the current density of 2 mA cm^{-2} for pure $CoMoO_4$/CC and hybrid $CoMoO_4$/PPy/CC electrode). In addition, the present value is also higher than other pseudo-capacitive materials such as WO_{3-x}/MoO_{3-x} Core/Shell Nanowires (0.5 F cm^{-2} at the current density of 2 mA cm^{-2})[40], Titanium dioxide@polypyrrole core–shell nanowires[19], TiO_2@MnO_2 nanowires (~62 mF cm^{-2} at 5 mA cm^{-2})[41], (~242 mF cm^{-2} at 1 mA cm^{-2})[42], etc. The results demonstrate that our electrode material possesses excellent electrochemical characteristics and can be very promising for supercapacitor electrodes. For comparison, the CV curves of pristine $CoMoO_4$/CC and $CoMoO_4$/PPy/CC electrode at the same scan rate of 50 mV s^{-1} are shown in the Figure 5e. The area of the CV curve enclosed from the $CoMoO_4$/PPy/CC composite electrode is much larger than that of the pristine $CoMoO_4$/CC electrode, which indicates that the electrochemical performance of the $CoMoO_4$/PPy/CC electrode has been greatly improved through the conductive wrapping method. CV curves of PPy/CC and pristine CC at the scan rate of 50 mV s^{-1} are displayed as Figure S1. To examine the ionic diffusion and electron transfer in the pure $CoMoO_4$ and core/shell $CoMoO_4$/PPy hybrid NWs, the Nyquist diagrams in the range of 100 kHz to 100 mHz are measured for both electrodes in a three-electrode configuration, as shown Figure 5f. The evident semicircle at high-frequency region responds to the ions and electron transfer characteristic of the electrode, which is related to the whole-electrode equivalent series resistance (ESR), electrolyte solution impedance, the inherent impedance of active material and the contact impedance between the electrode and electrolyte interface. The linear part appoints the Warburg impedance (Z_W), which is depicted as a frequency-dependent diffusion impedence of the ions between electrolyte and electrode surface. A slope of a nearly vertical line arises from higher frequency for $CoMoO_4$/PPy hybrid NWs than pure $CoMoO_4$ NWs, indicating the enhanced capacitive performance for the composite. Inset of Figure 5f shows the high-frequency domain of the Nyquist plots, $CoMoO_4$/PPy exhibits lower ESR than $CoMoO_4$, demonstrating that composite nanowires electrode possesses a lower diffusion resistance and significantly improved electronic/ionic conductivities. More detailed analysis of diffusion coefficients and warburg impedance has been shown as Fig S4 and Table S1. In a similar way, Fig S3 accurately confirms $CoMoO_4$/PPy hybrid NWs after 2000 cycles possess higher electronic/ionic conductivities than pure $CoMoO_4$ NWs, also demonstrating the PPy conductive layer enhanced the conductivities.

To further confirm that $CoMoO_4$ NWs wrapped on conductive coating PPy exhibit much better capacitance deliverability than single $CoMoO_4$ NWs electrode. Fig. 6a shows the relationship between the areal capacitance and the discharge current density. The highest areal capacitance of the $CoMoO_4$/PPy electrode is about 1.34 F cm^{-2} at a discharge current density of 2 mA cm^{-2}. Remarkably, the hybrid NWs electrode is much higher areal capacitance than pristine $CoMoO_4$ NWs electrode, especially at high current rates. The long-term cycle stability was tested by GCD at a current density of 4 mA cm^{-2} for 2000 cycles and the results are shown in Fig. 6b. It is obvious that the areal capacitance of $CoMoO_4$/PPy hybrid NWs is higher than that of pure $CoMoO_4$ NWs. The capacitance of the hybrid NWs only has a slight fluctuation in the whole process and the capacity retention is 95.2% (ca. 1.12 F cm^{-2}) after 2000 cycles and 98.6% (ca. 1.16 F cm^{-2}) for 1000 cycles, indicating an excellent cyclic stability. For bare $CoMoO_4$ NWs electrode, 82.4% capacitance (ca. 0.572 F cm^{-2}) is remained after 2000 cycles and 89% (ca. 0.527 F cm^{-2}) for 1000 cycles. Compared with nanocomposite electrode, it also has shown a good cyclic stability. Notably, the pure $CoMoO_4$ NWs suffer from relatively more capacitance loss for the first 1000 cycles, while the $CoMoO_4$/PPy nanocomposite assumes quite stable performance. This can be in part explained by the electrode's structural failure and detachment from current collector resulting from repeatedly mechanical stresses along with the electrochemical-reaction induced volumetric variations, the structural integrity and basic morphology of the NW arrays were described in Figure S2. The better cyclic stability of $CoMoO_4$/PPy nanocomposite is mainly attributed to the existence of PPy coating layer. First, the PPy shell could serve as a mechanical buffering layer that prevents the structural evolution of $CoMoO_4$ NWs during its charge/discharge cycling. Second, the PPy shell is able to tolerate the volumetric swelling and shrinking, acting as a conductive network to alleviate the electrode fragments and maintain their mechanical and electrochemical stability.[43]

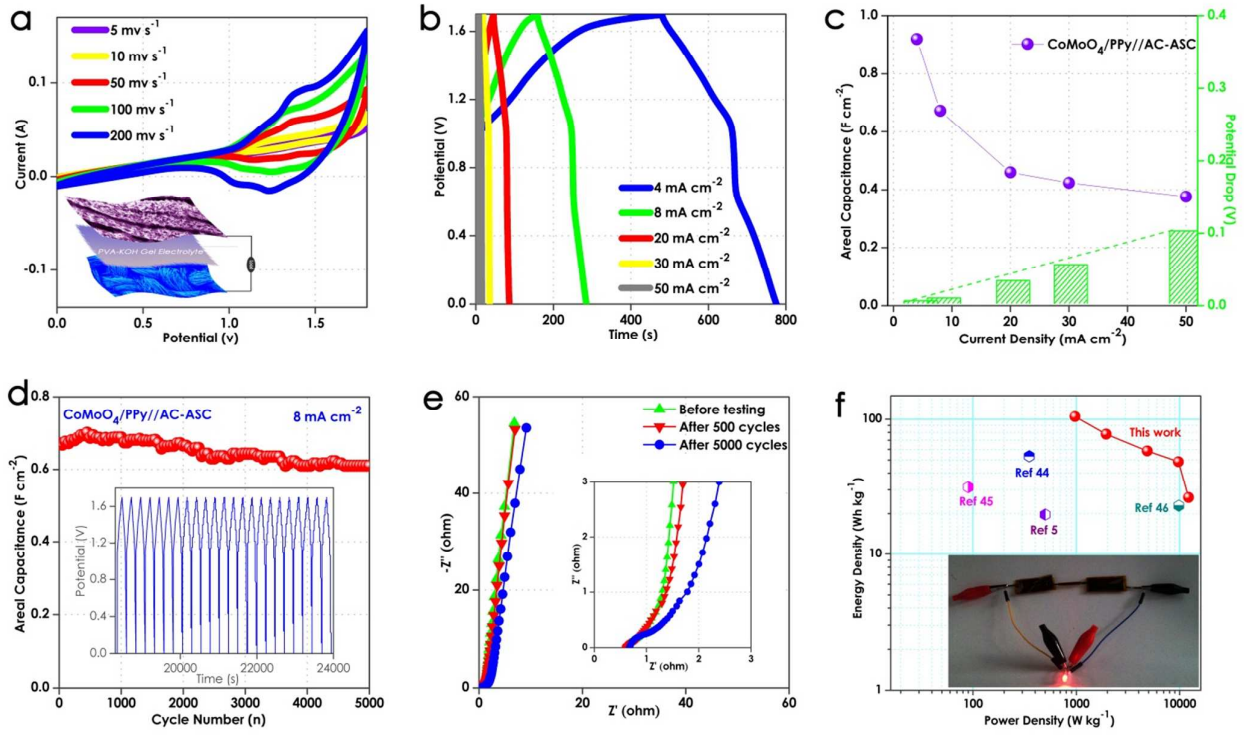

Fig. 7 Characteristics of the $CoMoO_4$/PPy/CC gel-based all-solid-state ASC. (a) CV curves measured at various scan rates (5 -200 mV s^{-1}), the inset in panel (a): schematic illustration of all-solid-state ASC. (b) GCD profiles measured at different current densities (4-50 mA cm^{-2}). (c) Areal capacitance and IR drop of the $CoMoO_4$/PPy//AC-ASC at different current densities. (d) Cyclic performance measurement of $CoMoO_4$/PPy//AC-ASC, the inset: charge/discharge profiles. (e) EIS plots of before and after 500, 5000 cycles. (f) Ragone plots of all-solid-state $CoMoO_4$/PPy//AC-ASC and comparable previous works.

Supercapacitors based on $CoMoO_4$/PPy//AC-PVA-KOH gel exhibited superb device characteristics for flexible energy-storage applications. Figure 7 reveals the constructions and electrochemical measurements outcomes of an as-packaged $CoMoO_4$/PPy//AC-ASC. The more rectangular-shaped CV curves of the $CoMoO_4$/PPy//AC-ASC compared to the individual $CoMoO_4$/PPy/CC electrode indicates excellent capacitive behaviors under the sweeping rates of 5−200 mV s^{-1} with an operating voltage of 0−1.7 V (Figure 7a). The inset of Figure 7a illustrates that the flexible all-solid-state ASC was assembled with $CoMoO_4$/PPy/CC nanostructured hybrid as the positive electrode and AC/CC as the negative electrode, as well as sandwiching a solid PVA-KOH gel electrolyte in-between. Figure 7b displays the GCD profiles of the all-solid-state $CoMoO_4$/PPy//AC-ASC devices collected under different current densities. The charge and discharge curves of the ASC device are analogically symmetric, which demonstrate favorable capacitive characteristics and rapid charge/discharge performance. Accordingly, Figure 7c shows the plots of areal specific capacitance and potential drop versus different discharge current densities for the ASC device. Along with the increment of current density up to 50 mA cm^{-2}, capacitance retention slightly reducing and IR potential drop marginally increasing, which effectively demonstrate the power output peculiarities of the $CoMoO_4$/PPy//AC-ASC. The long-term cycle stability of the ASC device under galvanostatic charge-discharge is another critical arguments for practical application, For $CoMoO_4$/PPy//AC-ASC device in Figure 7d over 5000 cycles between 0 and 1.7 V at a current density of 8 mA cm^{-2}, it was noticed that there was a gradual increment of the specific capacitance with the beginning of the cycles (around 1000 cycles), which can be attributed to the complete activation of the electrode materials. The areal specific capacitance of the $CoMoO_4$/PPy//AC-ASC device could reach a maximum value of 0.72 F cm^{-2} after activation. The bottom insets in Figure 7d were the twenty-three charge-discharge profiles for the GCD cycles. This further demonstrated that the all-solid-state $CoMoO_4$/PPy//AC-ASC device has a good cyclic stability. In additional, Fig. 7e shows the Nyquist impedance spectra of the ASC device before and after 500 and 5000 cycles, respectively. Remarkably, the EIS spectra before and after 500 cycles are similar in terms of the plot shape except that an inconspicuous change of the Warburg impedance (Z_W) depicted as a frequency-dependent diffusion impendence of the ions from electrolyte to electrode surface in the low frequency range, indicating that the as-fabricated ASC devices have a relatively good stability after 500 cycles. However, the ESR and Z_W obtained for the asymmetric supercapacitors after 5000 cycles have taken place evident changes compared with before and after 500 cycles, probably resulting from the $CoMoO_4$/PPy NWs collapsing severely block efficient electrons and ions transportation between the electrode and electrolyte during

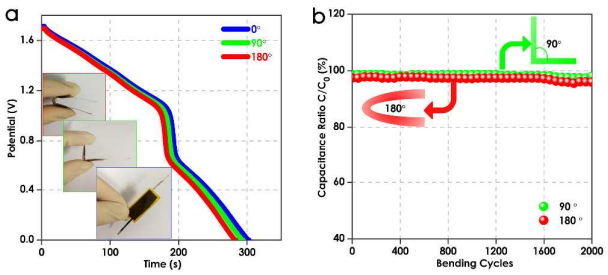

Fig. 8 Comparisons of the $CoMoO_4$/PPy/CC gel-based all-solid-state ASC under the different bent states (a) GCD profiles at 4 mA cm^{-2}. The inset : flat ASC(blue), bent ASC at 90° (green) and 180° (red), (b) Capacity retention after 2000 charge–discharge cycles at the current density of 8 mA cm^{-2}.

charge-discharge processes as well as corresponding to the impedance testing. The power and energy density of the ASC device under various applied currents are displayed in Figure 7f. The maximum energy density as high as 104.7 Wh kg^{-1} (3.522 mWh cm^{-3}) is obtained at a current density of 4 mA cm^{-2} with power density of 971.43 W kg^{-1} (32.6 mW cm^{-3}) under the operating voltage of 1.7 V. The flexible ASC device possesses a maximum of 12171.3 W kg^{-1} (409.6 mW cm^{-3})power density at the current density of 50 mA cm^{-2} with energy density of 26.37 Wh kg^{-1} (0.887 mWh cm^{-3}). These results demonstrate huge improvements exceeding a number of previously reported values from all-solid-state supercapacitors. Furthermore, to demonstrate the practical application of the asymmetric supercapacitor device, a red light-emitting diode (LED) can be lit by the all-solid-state flexible ASC device (as shown inset of figure 7f).

To study the outstanding flexibility of all-solid-state ASC device influence on the electrochemical performance, we compared the GCD curves and cyclic performance of the $CoMoO_4$/PPy hybrid NWs based flexible ASC under flat and angles of ca. 90° and 180° bent states, as indicated in Figure 8. The GCD profiles presented in Figure 8a confirm the slight attenuation of charge-discharge interval of the bent ASC compared to its flat state. Figure 8b shows the capacitance ratio (i.e., a ratio of the capacitance under a bent state to that at natural) as a function of the bending cycles at a current density of 8 mA cm^{-2}. From Figure 8b, the capacitance ratio of a bending angle of ca. 90° ASC device attains 98% before 1500 cycles, then decreases to 96% over 2000 cycles. Similarly, ASC device of a bending angle of ca. 180° achieves a capacitance ratio of 97% around 1500 cycles, which then decreases to 95% after 2000 cycles. These results may be attributable to structural damage of the $CoMoO_4$/PPy hybrid NW arrays under these harsh mechanical stress conditions. However, the excellent mechanical robustness and intimate interfacial contact for the multiple components demonstrate their promising utility as a flexible energy storage device.

Conclusions

In summary, we have successfully synthesized uniform $CoMoO_4$/PPy core-shell NW arrays with evenly distributed dimensions as the main pseudocapacitive active materials on highly conductive CC substrates by a facile two-step method. 1D core-shell nanowire-array structures endow the $CoMoO_4$/PPy nanocomposites with excellent mechanical flexibility, good specific capacitance and excellent cyclic stability. Furthermore, we also assembled a flexible all-solid-state ASC device based on the $CoMoO_4$/PPy hybrid NWs electrode. The ASC device clearly indicates excellent capacitive properties, high cyclic stability and outstanding flexibility. Even under a bending angle of up to 180°, the capacitance ratio of the ASC reaches 95% for over 2000 charge/discharge cycles. These significant properties render the flexible ASC device with a relatively high energy density and power density. Our study highlights the great potential for a flexible all-solid-state ASC device as energy-storage for various portable, flexible and wearable electronic applications.

Acknowledgements

This work was supported by National Natural Science Foundation of China (21353003), Special Innovation Talents of Harbin Science and Technology (2013RFQXJ145), Fundamental Research Funds of the Central University (HEUCFZ), Natural Science Foundation of Heilongjiang Province (B201316), Program of International S&T Cooperation special project (2015DFR50050), and the fund for Transformation of Scientific and Technological Achievements of Harbin (2013DB4BG011).

References

1. P. S. Y. Gogotsi, Nat. Mater. 2008.
2. Z. Qian, T. Peng, J. Wang and L. Qu, ChemSusChem, 2014, 7, 1881-1887.
3. R. A. Davoglio, S. R. Biaggio, N. Bocchi and R. C. Rocha-Filho, Electrochimica. Acta, 2013, 93, 93-100.
4. J. Chen, L. Yang, S. Fang and Y. Tang, Electrochimica. Acta, 2010, 55, 6596-6600.
5. B. G. Choi, S. J. Chang, H. W. Kang, C. P. Park, H. J. Kim, W. H. Hong, S. Lee and Y. S. Huh, Nanoscale, 2012, 4, 4983-4988.
6. K. M. Hercule, Q. Wei, O. K. Asare, L. Qu, A. M. Khan, M. Yan, C. Du, W. Chen and L. Mai, Adv. Energy Mater. 2015, 5, n/a-n/a.
7. J. Liu, J. Jiang, C. Cheng, H. Li, J. Zhang, H. Gong and H. J. Fan, Adv. Mater. 2011, 23, 2076-2081.
8. X. H. Xia, D. L. Chao, Z. X. Fan, C. Guan, X. H. Cao, H. Zhang and H. J. Fan, Nano Lett. 2014, 14, 1651-1658.
9. J. Xu, Q. Wang, X. Wang, Q. Xiang, B. Hang, D. Chen and G. Shen, Acs Nano, 2013, 7, 5453-5462.
10. M. L. Huang, C. D. Gu, X. Ge, X. L. Wang and J. P. Tu, J. Power Sources. 2014, 259, 98-105.
11. J. Bao, X. D. Zhang, L. F. Bai, W. C. Bai, M. Zhou, J. F. Xie, M. L. Guan, J. F. Zhou and Y. Xie, J. Mater. Chem. A. 2014, 2, 10876-10881.
12. W. Yang, Z. Gao, J. Ma, X. Zhang, J. Wang and J. Liu, J. Mater. Chem. A. 2014, 2, 1448.
13. L. Q. Mai, F. Yang, Y. L. Zhao, X. Xu, L. Xu and Y. Z. Luo, Nat. Commun. 2011, 2, 381.

14. X. Yu, B. Lu and Z. Xu, Adv. Mater. 2014, 26, 1044-1051.
15. H. Yu, C. Guan, X. Rui, B. Ouyang, B. Yadian, Y. Huang, H. Zhang, H. E. Hoster, H. J. Fan and Q. Yan, Nanoscale, 2014, 6, 10556-10561.
16. D. Cai, B. Liu, D. Wang, Y. Liu, L. Wang, H. Li, Y. Wang, C. Wang, Q. Li and T. Wang, Electrochimica Acta, 2014, 125, 294-301.
17. K. Zhang, L. L. Zhang, X. S. Zhao and J. S. Wu, Chem. Mat. 2010, 22, 1392-1401.
18. L. Zhang, K. Zhao, W. Xu, Y. Dong, R. Xia, F. Liu, L. He, Q. Wei, M. Yan and L. Mai, *Phys. Chem. Chem. Phys.* 2015, 17, 7619-7623.
19. M. Yu, Y. Zeng, C. Zhang, X. Lu, C. Zeng, C. Yao, Y. Yang and Y. Tong, Nanoscale, 2013, 5, 10806-10810.
20. X. Xia, D. Chao, Z. Fan, C. Guan, X. Cao, H. Zhang and H. J. Fan, Nano Lett. 2014, 14, 1651-1658.
21. Q. Zhang, E. Uchaker, S. L. Candelaria and G. Cao, Chem. Soc. Rev. 2013, 42, 3127-3171.
22. Y. Zhao, B. Liu, L. Pan and G. Yu, Energy Environ. Sci. 2013, 6, 2856.
23. J. R. Miller and P. Simon, Science, 2008, 321, 651-652.
24. J. Jiang, J. Zhu, W. Ai, Z. Fan, X. Shen, C. Zou, J. Liu, H. Zhang and T. Yu, Energy Environ. Sci. 2014, 8, 2670-2679.
25. B. R. Liu, P. Soares, C. Checkles, Y. Zhao and G. H. Yu, Nano Lett. 2013, 13, 3414-3419.
26. P. Chiu and I. Shih, Nanotechnology, 2004, 15, 1489-1492.
27. L. Cademartiri, F. Scotognella, P. G. O'Brien, B. V. Lotsch, J. Thomson, S. Petrov, N. P. Kherani and G. A. Ozin, Nano Lett. 2009, 9, 1482-1486.
28. S. Barth, M. M. Kolesnik, K. Donegan, V. Krstic and J. D. Holmes, Chem. Mat. 2011, 23, 3335-3340.
29. M. M. Gabriel, E. M. Grumstrup, J. R. Kirschbrown, C. W. Pinion, J. D. Christesen, D. F. Zigler, E. E. M. Cating, J. F. Cahoon and J. M. Papanikolas, Nano Lett. 2014, 14, 3079-3087.
30. B. Wang, X. Y. He, H. P. Li, Q. Liu, J. Wang, L. Yu, H. J. Yan, Z. S. Li and P. Wang, J. Mater. Chem. A. 2014, 2, 12968-12973.
31. P. Yu, Y. Li, X. Yu, X. Zhao, L. Wu and Q. Zhang, Langmuir : the ACS journal of surfaces and colloids, 2013, 29, 12051-12058.
32. Z. Sun, S. Firdoz, E. Y. Yap, L. Li and X. Lu, Nanoscale, 2013, 5, 4379-4387.
33. F. Tao, M. Guan, Y. Jiang, J. Zhu, Z. Xu and Z. Xue, Adv. Mater. 2006, 18, 2161-+.
34. R. A. DiLeo, S. Frisco, M. J. Ganter, R. E. Rogers, R. P. Raffaelle and B. J. Landi, J. Phys. Chem. C. 2011, 115, 22609-22614.
35. Y. Wang, Y. Wang, D. Jia, Z. Peng, Y. Xia and G. Zheng, Nano Lett. 2014, 14, 1080-1084.
36. X. Lu, M. Yu, G. Wang, T. Zhai, S. Xie, Y. Ling, Y. Tong and Y. Li, Adv. Mater. 2013, 25, 267-272.
37. J. Rodriguez-Moreno, E. Navarrete-Astorga, E. A. Dalchiele, R. Schrebler, J. R. Ramos-Barrado and F. Martin, Chem. Commun. 2014, 50, 5652-5655.
38. G. H. Zhang, S. C. Hou, H. Zhang, W. Zeng, F. L. Yan, C. C. Li and H. G. Duan, Adv. Mater. 2015, 27, 2400-2405.
39. J. S. Lee, D. H. Shin, J. Jun and J. Jang, Acs Nano, 2013, 7, 10139-10147.
40. X. Xiao, T. Ding, L. Yuan, Y. Shen, Q. Zhong, X. Zhang, Y. Cao, B. Hu, T. Zhai, L. Gong, J. Chen, Y. Tong, J. Zhou and Z. L. Wang, Adv. Energy Mater. 2012, 2, 1328-1332.
41. R. Liu, J. Duay and S. B. Lee, Acs Nano, 2010, 4, 4299-4307.
42. J. W. Lee, A. S. Hall, J. D. Kim and T. E. Mallouk, Chem. Mat. 2012, 24, 1158-1164.
43. T. Liu, L. Finn, M. Yu, H. Wang, T. Zhai, X. Lu, Y. Tong and Y. Li, Nano Lett. 2014, 14, 2522-2527.
44. Y. He, W. Chen, J. Zhou, X. Li, P. Tang, Z. Zhang, J. Fu and E.Xie, ACS Appl. Mater. Interfaces. 2014, 6, 210-218.
45. P. Tang, L. Han and L. Zhang, ACS Appl. Mater. Interfaces. 2014, 6, 10506-10515.
46. P. Yu, Y. Li, X. Yu, X. Zhao, L. Wu and Q. Zhang, Langmuir, 2013, 29, 12051-12058.

Table of Contents (TOC) Images